

Pressure-Induced Phase Changes in Cesium Lead Bromide Perovskite Nanocrystals with and without Ruddlesden–Popper Faults

Sorb Yesudhas, Maria V. Morrell, Matthew J. Anderson, Carsten A. Ullrich, Curtis Kenney-Benson, Yangchuan Xing, and Suchismita Guha*



Cite This: *Chem. Mater.* 2020, 32, 785–794



Read Online

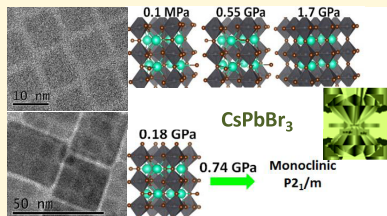
ACCESS |

Metrics & More

Article Recommendations

Supporting Information

ABSTRACT: Lead halide perovskites have a rich landscape of structural and optical properties, which can be explored and possibly controlled by applying high pressure. Despite several reports on high-pressure studies of CsPbBr_3 nanocrystals (NCs), there have so far been no studies under pressure that incorporate planar defects. CsPbBr_3 NCs with Ruddlesden–Popper (RP) faults, formed via post-synthetic fusion growth, are significantly larger in size than as-synthesized NCs and display exceptional emission stability. Here, we compare synchrotron-based high-pressure X-ray diffraction and photoluminescence (PL) properties of CsPbBr_3 (without RP) and RP- CsPbBr_3 (with RP) and resolve their crystal structure under pressure for the first time. CsPbBr_3 undergoes a phase transition from the orthorhombic $Pnma$ phase at ambient pressure to the cubic $Pm\bar{3}m$ phase at 1.7 GPa, and RP- CsPbBr_3 transforms from $Pnma$ to the monoclinic $P2_1/m$ phase at 0.74 GPa in addition to several isostructural transitions. Density-functional calculations predict a narrowing of the band gap with pressure, concomitant with the PL energies. The RP- CsPbBr_3 NCs exhibit enhanced PL intensity at 1 GPa and show band gap opening at high pressures. This study opens new strategies for not only tuning just the structural properties but also tuning planar defects in alkali halide lead crystals for improved optical properties.



INTRODUCTION

On account of their superior stability, high photoluminescence (PL) quantum yield, prolonged carrier lifetimes, and narrow emission bandwidths over hybrid (organic–inorganic) halide perovskites, all inorganic cesium lead halide perovskite (CsPbX_3 , $X = \text{Br, Cl or I}$) nanocrystals are attracting much attention as low-cost, high-performing semiconductors for optoelectronics.^{1–6} Similar to hybrid halide perovskites, the CsPbX_3 family offers tunability in its optical band gap energy through compositional changes. Since CsPbX_3 can be easily synthesized as nanocrystals (NCs), the optical properties may be further tuned by size effects.

The halide perovskites have a rich phase diagram. Conventionally, CsPbBr_3 stabilizes as untilted aristotype $Pm\bar{3}m$ (Glazer tilt notation: $a^0a^0a^0$) cubic perovskite structure at 130 °C as a result of corner sharing of $[\text{PbBr}_6]^{4-}$ octahedra in all three directions, producing 3D infinite $[\text{PbBr}_3]^-$ frameworks where the Cs atoms fill the cuboctahedral cavities.^{1,7,8} Upon cooling to around 88 °C, the material undergoes a symmetry lowering phase transition to a tetragonal structure with $P4/mbm$ symmetry [Glazer tilt notation: $a^0a^0c^+$] due to the in-phase rotations of PbBr_6 octahedra along the c -axis. Upon further cooling to the ambient, the symmetry lowers again to an orthorhombic structure with $Pnma$ symmetry [Glazer tilt notation: $a^+b^-b^-$] by the additional rotations of octahedra along a and b axes.^{9–11}

Hydrostatic pressure offers a systematic control for tuning structure and thus the optical and electronic properties of metal halide perovskites, without any chemical intervention. This technique not only yields insights into structural and other aspects of materials at elevated pressures^{12,13} but also for NCs, as we see here, applying a small pressure can enhance the PL. Additionally, the tunability of optical and electronic properties under pressure presents avenues for a feedback loop for improved synthesis of materials. There have been several high-pressure studies reported on CsPbX_3 NCs using X-ray diffraction (XRD), Raman scattering, optical absorption, and PL studies;^{14–17} however, to-date, the high-pressure phases are not completely resolved.

Pressure-dependent structural and optical changes in orthorhombic CsPbBr_3 NCs have been attributed to an isostructural transition at ~ 1 GPa owing to the changes in Pb–Br bond lengths and also due to the distortion of the PbBr_6 octahedra.¹⁷ The band gap changes under pressure in CsPbBr_3 NCs are typically accompanied by a dramatic reduction of the PL intensity on account of a loss of long-range order, rendering the system to an amorphous state

Received: October 10, 2019

Revised: December 24, 2019

Published: December 26, 2019

caused by the tilting and distortion of the octahedra.¹⁴ Using small- and wide-angle synchrotron X-ray scattering combined with PL studies, Nagaoka et al. observed that a mixture of cubic and orthorhombic CsPbBr_3 NCs at ambient conditions undergoes a pressure-induced structural phase transition to a pure orthorhombic phase at 0.4 GPa and afterward to a quasi-amorphous phase around 5 GPa.¹⁸ A theoretical report predicts the orthorhombic phase of CsPbBr_3 to undergo a structural phase transition to hexagonal symmetry at 13 GPa through intermediate lower symmetry phases.¹⁹ There are further predictions of a paraelectric to ferroelectric transition at 15 GPa.²⁰

There have been recent reports on CsPbBr_3 NCs with Ruddlesden–Popper (RP) faults,^{21–23} which thus far had been only observed in 3D oxide perovskites,^{24,25} and in other 2D organic–inorganic layered perovskites with high photovoltaic and light-emitting diode efficiencies.^{26,27} Density-functional theory (DFT) calculations show that planar defects such as grain boundaries and RP faults in CsPbBr_3 do not show any deep defect levels, provided there are no Pb dangling bonds, but they can produce band offsets and affect charge-transport properties.²³ In fact, the presence of RP faults in CsPbBr_3 NCs is seen to greatly enhance the PL quantum yield and enhance stability against photodegradation.²² The CsPbBr_3 NCs with RP faults may grow up to 60 nm in the lateral dimension during the postsynthesis treatment compared to approximately 8 nm lateral dimension for regular NCs. The RP faults appear due to the incorporation of a CsBr layer between CsPbBr_3 domains; the two adjacent CsBr layers are shifted with respect to each other by half a unit cell.

Thus far, there are no high-pressure structural and optical investigations of CsPbBr_3 NCs with RP faults. Here, we compare synchrotron-based XRD and PL studies from CsPbBr_3 NCs (~ 8 nm) and CsPbBr_3 NCs (~ 35 nm) with RP faults. The nomenclature used here is CsPbBr_3 for NCs (without RP faults) and the RP- CsPbBr_3 for NCs with the presence of RP faults. Although the structure under ambient conditions indicates that both samples are orthorhombic, the structural evolution under pressure is different for the two NCs. We resolve the high-pressure phase of orthorhombic CsPbBr_3 and further confirm the experimental PL results with DFT calculations. First-principles calculations reveal a narrowing of the band gap with increasing pressure. Since we have refined the lattice parameters and Wyckoff positions for various pressure values from the XRD data, we use the experimental input for first-principles calculations. The simulated band gap energy under pressure shows a similar trend as the experimental PL energies, further highlighting a self-consistent structure–property prediction under pressure.

Although the PL energy red-shifts at low pressures for both CsPbBr_3 and RP- CsPbBr_3 NCs, the pressure coefficients are different. The RP- CsPbBr_3 sample shows an increase in the PL energy beyond 0.8 GPa, whereas the CsPbBr_3 sample continues to red-shift till 1.3 GPa, beyond which the PL emission disappears. The PL intensity for RP- CsPbBr_3 is seen to greatly enhance at ~ 1 GPa compared to the ambient. More than just a tuning parameter, our results suggest that pressure studies could provide insights into the crystallographic phases of other alkali halide NCs that have planar defects and direct synthesis to mimic the high-pressure phase for improved optical properties.

EXPERIMENTAL/THEORETICAL SECTION

Nanocrystal Growth. CsPbBr_3 nanocrystals were prepared following the procedure reported by Protesescu et al.² Cs -oleate was injected into a mixture, containing PbBr_2 , oleic acid, oleylamine, and octadecene, under a N_2 atmosphere at 185 °C. Immediately after injection, the mixture was cooled with an ice-water bath. Nanocrystals were collected by centrifugation at 4000 rpm for 12 min. Ruddlesden–Popper planar faults were formed in CsPbBr_3 nanocrystals by introducing diethyl zinc in the glovebox under an Ar atmosphere at room temperature.²² Detailed synthesis procedure and experimental evidence of the NCs with RP faults using high-resolution scanning tunneling microscopy are provided in refs 22, 23.

Instrumentation and Methods. High-pressure experiments were carried out using both symmetric and Merrill–Bassett-type diamond anvil cells (DACs). The culet sizes of the symmetric and the Merrill–Bassett-type DACs used were 400 and 600 μm , respectively. A stainless-steel gasket was preindented to a thickness of 60 μm with diamond anvils, and a hole of diameter about 180 μm was drilled at the center using a laser drilling machine, which acts as the pressure chamber. The pressure was determined using the standard ruby fluorescence technique. The pressure-transmitting medium was neon.

Temperature- (T) and pressure-dependent PL measurements were carried out in reflection and transmission modes, respectively. Low-temperature PL studies were carried in a closed-cycle CTI refrigerator using the 325 nm wavelength of a HeCd laser as the excitation source at a power of < 10 mW on the sample, and the PL spectra were collected using Ocean Optics USB 2000. High-pressure PL studies were carried using the 457 nm line from an Ar^+ ion laser as the excitation source; silicone oil was used as a pressure-transmitting medium. The pressure was determined by using Renishaw in via a Raman spectrometer with 514 nm Ar^+ ion laser as the excitation source. The spectral resolution of the instrument is lower than 0.2 cm^{-1} , which results in pressure uncertainties being lower than 0.05 GPa. PL measurements were carried by Merrill–Bassett-type DAC, and the hydrostatic condition was achieved by loading silicone oil inside the sample chamber.

High-resolution transmission electron microscope (TEM) images were obtained with an FEI Tecnai F30 Twin 300 kV.

High-Pressure Synchrotron XRD. High-pressure angle dispersive synchrotron XRD (ADXRD) experiments were carried out at 16-BMD, HPCAT, Advanced Photon Source (APS), Argonne National Laboratory. The wavelengths of X-ray used were 0.4133 and 0.4959 \AA . Ne gas was used as a pressure-transmitting medium, and it was loaded at GSECARS, Sector 13, APS. The sample to detector distance was calibrated using CeO_2 , and the XRD image was collected by an image plate detector. The 2D image was integrated to obtain the 1D intensity vs 2θ data by the Fit2d software.²⁸ The lattice parameters were calculated from the XRD pattern by Rietveld refinement and profile matching using the FullProf Suite software.²⁹ The lattice parameters and U , V , and W width parameters, zero correction, background, and the Wyckoff positions are refined until the goodness of fit conditions are achieved. The profile parameters were varied by using the least square minimization method. A pseudo-Voight function was used as a peak shape function. The profile parameters: R_p , R_{Wp} , R_B , and χ^2 values were used as guidance to achieve the goodness of fit. The crystal structures were plotted using VESTA.

Computational Details. The band-structure calculations were performed using plane-wave pseudopotentials as implemented in the ABINIT electron structure code.^{30,31} The core electrons were eliminated from the calculation using norm-conserving pseudopotentials generated by ONCVPSP.³² We chose the functional developed by Perdew, Burke, and Ernzerhof (PBE) as the exchange-correlation functional³³ and used a cutoff energy of 20 Ha (544 eV). A reciprocal space sampling of an $8 \times 8 \times 8$ Monkhorst–Pack mesh³⁴ with a Γ center was used for all calculations. The input structures for all of the calculations were from the solved structures based on XRD data. The only exception was the cubic phase, where the higher-pressure data points were simulated using the experimental change in volume (for

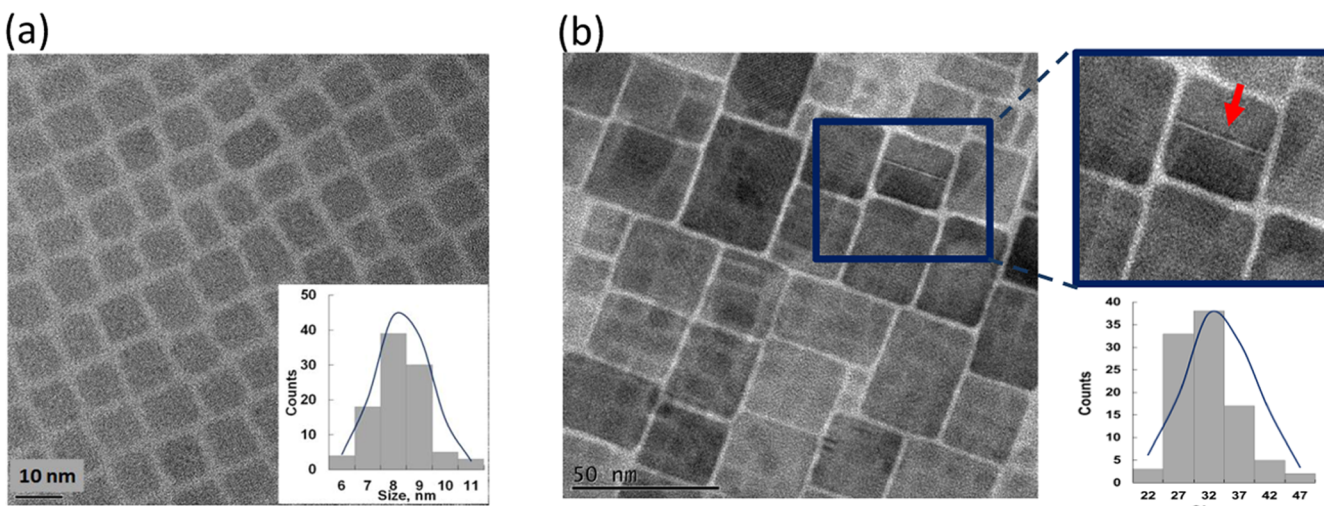


Figure 1. TEM images of CsPbBr_3 NCs with and without RP planar faults. (a) High-resolution TEM image of CsPbBr_3 NCs. The size distribution profile is shown as an inset at the bottom right. The average size of the NCs is about 8 nm. (b) TEM image of RP- CsPbBr_3 NCs with a close-up image of an RP fault (top) depicted by the red arrow and the size distribution profile (bottom). The average size is about 32 nm.

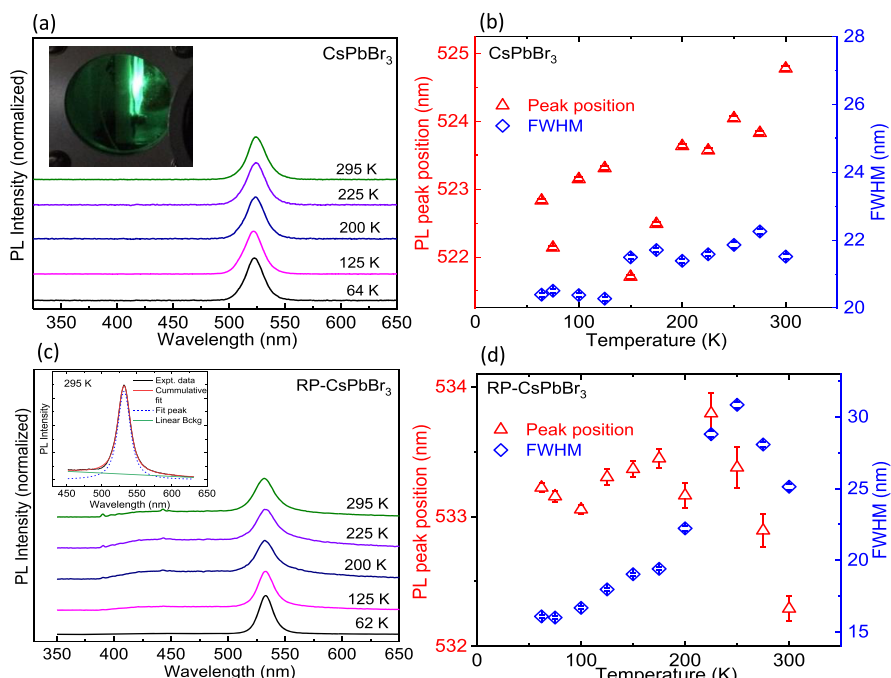


Figure 2. Temperature-dependent PL spectra of CsPbBr_3 NCs. (a) PL spectra of CsPbBr_3 NCs at selected temperatures. The inset shows an optical image of the PL through a cryostat window. (b) The temperature dependence of PL peak position and full width at half-maximum (FWHM) of CsPbBr_3 NCs. (c) PL spectra of RP- CsPbBr_3 NCs at selected temperatures. The inset shows a fit to the 295 K PL data with a Gaussian peak and a linear background. (d) The temperature dependence of PL peak position and FWHM of RP- CsPbBr_3 NCs. The error bars are from the Gaussian-fitting uncertainty.

the orthorhombic phase) under pressure. No structural relaxations were performed.

RESULTS AND DISCUSSION

TEM Images. Detailed characterization and analysis of RP faults are provided in refs 22, 23. Figure 1a,b shows high-resolution TEM images of CsPbBr_3 and RP- CsPbBr_3 used in the high-pressure experiments. The average size of RP- CsPbBr_3 is ~ 32 nm compared to 8 nm for CsPbBr_3 NCs. Figure 1b shows a close-up image of an RP fault. Additional evidence of RP faults using high-angle annular dark-field images is provided in the Supporting Information (Figure S1).

Temperature-Dependent PL Measurements. The PL spectrum of CsPbBr_3 NCs is characterized by a narrow peak in the green region of the spectrum. Figure 2 shows the normalized PL spectra from thin-film samples that were cast from CsPbBr_3 and RP- CsPbBr_3 samples at selected temperatures. There is a slight bathochromic shift in the PL spectra since they are thin-film samples compared to the PL from colloidal solutions in ref 22. The PL peak was fitted with a Gaussian peak to obtain the peak position and the full width at half-maximum (FWHM); a sample fit is shown in Figure 2c (inset). As expected, due to the larger size of NCs in RP- CsPbBr_3 compared to CsPbBr_3 NCs, the PL energy is red-

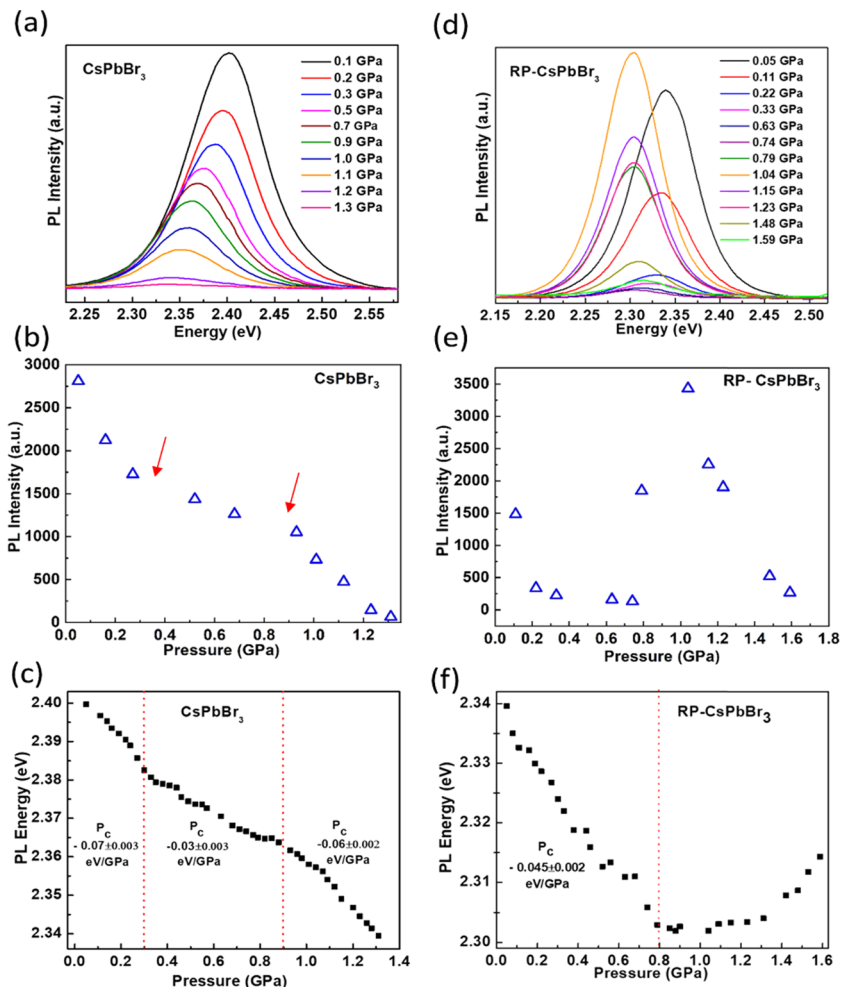


Figure 3. Pressure-dependent PL spectra, intensity, and energy of CsPbBr₃ and RP-CsPbBr₃. (a) Pressure-dependent PL spectra of CsPbBr₃ NCs for selected pressures. (b) PL intensity of CsPbBr₃ NCs for selected pressures. The slanted red arrows indicate the inflection points. (c) PL energy versus pressure of CsPbBr₃ NCs. The linear pressure coefficient (P_c) is denoted for the three regions. The dotted lines represent the pressure values where the pressure coefficient changes. (d) Pressure-dependent PL spectra of RP-CsPbBr₃ NCs for selected pressures. (e) PL intensity of RP-CsPbBr₃ NCs for selected pressures. (f) PL energy versus pressure for RP-CsPbBr₃ NCs.

shifted. Despite the significant size increase in RP-NCs, the luminescence shows a relatively small red-shift compared to NCs, which we believe is due to the RP-induced quantum confinement effect and not due to any 2D nanostructures. There is hardly any change in the PL peak position (within ± 2 nm) for either of the samples in the temperature range of 60–300 K. These results are consistent with a homogeneous particle size distribution along with quantum confinement effects in both samples. We note that the temperature dependence of the PL spectra observed here contrasts several works, where due to the large particle size, a significant shift in the PL peak position with temperature was observed.^{35,36}

Despite the small shifts in the PL energy as a function of temperature, some differences are observed between CsPbBr₃ and RP-CsPbBr₃. Except for an anomaly in the peak position at ~ 200 K, the overall trend in CsPbBr₃ is a red-shift in PL energies with increasing temperature (note that the PL peak positions are plotted in nm and not in eV). The red-shift in energy with temperature is typical of quantum wells and bulk semiconductors due to a renormalization of band energies by electron–phonon interactions.³⁷ In semiconducting quantum dots, however, depending on the size distribution, the PL energies often blue-shift due to a loss of carriers from the larger

quantum dots that have lower energies to the smaller quantum dots with higher energies.³⁸

To get further insight into the changes in PL, we have carried out laboratory-based low-temperature XRD until 90 K in CsPbBr₃ NCs. Temperature dependences of both lattice parameters and volume exhibit an anomaly at ~ 230 K; a detailed description is provided in the Supporting Information. Furthermore, a recent Raman scattering study from CsPbBr₃ NCs as a function of temperature shows an order–disorder transition around 200 K,³⁹ therefore, the observed anomaly in the PL at ~ 200 K could be related to this transition. The PL energy in RP-CsPbBr₃ remains almost unchanged till 250 K, beyond which there is a slight blue-shift (of ~ 7 meV between 250 and 300 K). The origin of this shift is not clear, although it is conceivable that it is a signature of a phase transition. As seen later, pressure-induced structural transitions in RP-CsPbBr₃ and CsPbBr₃ have differences; hence, temperature-dependent phase transitions for the two samples may also vary.

Although RP-CsPbBr₃ has a broader size distribution compared to CsPbBr₃, the FWHM is narrow, especially at low temperatures, which has been attributed to the retention of quantum confinement in the smaller domains within the large domains.²² The effective Bohr radius for CsPbBr₃ is estimated

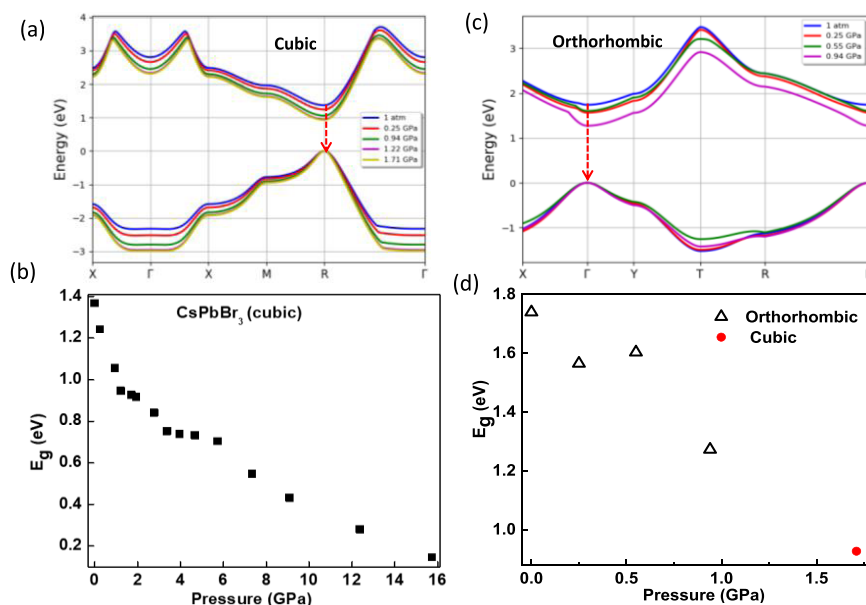


Figure 4. Calculated band structure and band gap of CsPbBr₃ as a function of pressure. (a) The electronic band edges of cubic CsPbBr₃ at selected pressures. (b) The band gap energy of cubic CsPbBr₃ as a function of pressure. (c) The electronic band edges of orthorhombic CsPbBr₃ at selected pressures. (d) The band gap energy of the orthorhombic phase as a function of pressure. The red circle corresponds to the band gap of the cubic phase at 1.7 GPa to correlate with the experimental observation.

to be ~ 7 nm;² hence, the sample without RPs is close to this limit. For the RP-CsPbBr₃ sample, these results further confirm the confinement of excitons in the small grains due to RP faults.

Pressure-Dependent PL Measurements. Figure 3a plots the PL spectra of CsPbBr₃ NCs at selected pressure values. Since the same geometry and incident intensity of the excitation laser were used for each measurement, the intensities are comparable. The PL intensity decreases with pressure with two inflections at 0.3 and 0.9 GPa, as shown in Figure 3b. The PL spectra under pressure were fitted with Gaussian line shapes to obtain the peak positions, which are plotted in Figure 3c. The PL energies (eV) are found to systematically red-shift and exhibit two inflection points at ~ 0.3 and ~ 0.9 GPa. The linear pressure coefficient (P_c) was obtained from $E(P) = E(0) + P_c P$, where $E(P)$ and $E(0)$ are the PL energies at pressure P and ambient pressure, respectively. The disappearance of the PL peak above 1.3 GPa can possibly be attributed to a structural phase transition as discussed with the analysis of the XRD data. Moreover, the anomaly at 0.9 GPa is concomitant with a broadening of the PL peak, an indicator of a precursor to a structural phase transition that is completed by 2.0 GPa. We note the PL intensity follows a similar trend as the PL energy with pressure.

The RP-CsPbBr₃ NCs exhibit a different PL behavior under pressure compared to CsPbBr₃ NCs. Initially, the PL intensity decreases with pressure, as shown in Figure 3d,e. At 1 GPa, the PL spectrum becomes quite intense, even stronger than under ambient conditions. Beyond this pressure value, the PL intensity again decreases and finally disappears around 1.6 GPa. Figure 3f plots the PL peak position (in eV), which systematically red-shifts till 0.8 GPa and then steadily blue-shifts; beyond 1.6 GPa, the PL peak completely disappears.

Another batch of CsPbBr₃ NCs (without RPs) was also measured, and the PL energies red-shift with pressure. This contrasts several reports on CsPbBr₃ NCs.^{14,17,18} A hint of an increasing optical band gap with pressure is only observed in

RP-CsPbBr₃. The PL spectra show reversibility upon decreasing the pressure (Figure S2), although there is some hysteresis.

Band-Structure Calculations. To get a deeper insight into the changes in the electronic structure with pressure, DFT calculations were performed to investigate the evolution of the electronic bands using the crystallographic information file (CIF) from CsPbBr₃ under pressure obtained from the experimental XRD measurements. Although the general consensus is that CsPbBr₃ NCs stabilize in the orthorhombic phase under atmospheric conditions,^{40,41} there are reports of the cubic or mixed orthorhombic and cubic phases.^{2,18} We thus estimate the change in the band gap of a purely cubic phase where the pressure effects on the band structure of this phase were simulated in accordance with the observed volume change for the (orthorhombic) sample. Figure 4 shows the calculated band structures and the extracted band gap energies (E_g) of cubic and orthorhombic CsPbBr₃ as a function of pressure. Since the PBE functional underestimates the band gap energy, our calculated band gap values are lower than the experimentally observed values, although they agree very well with recent theoretical calculations.¹⁹ The orthorhombic and cubic phases of CsPbBr₃ are direct band gap at Γ and R symmetric points (Figure 4a,c) of the Brillouin zone, respectively. Since the orthorhombic phase transforms to the cubic phase beyond 1.5 GPa, as discussed later with the XRD data analysis, the value of E_g at 1.7 GPa (in Figure 4d) corresponds to the cubic phase. The trends in E_g versus pressure agree well with the experimental PL data, which further highlights the consistency in structure prediction of the high-pressure phases of CsPbBr₃.

The blue shift seen in the experimental PL data of RP-CsPbBr₃ above 0.8 GPa most likely originates from the monoclinic structural phase transition along with the presence of RP faults. An opening of the band gap with pressure is not predicted from theory in the pressure range of the calculations.

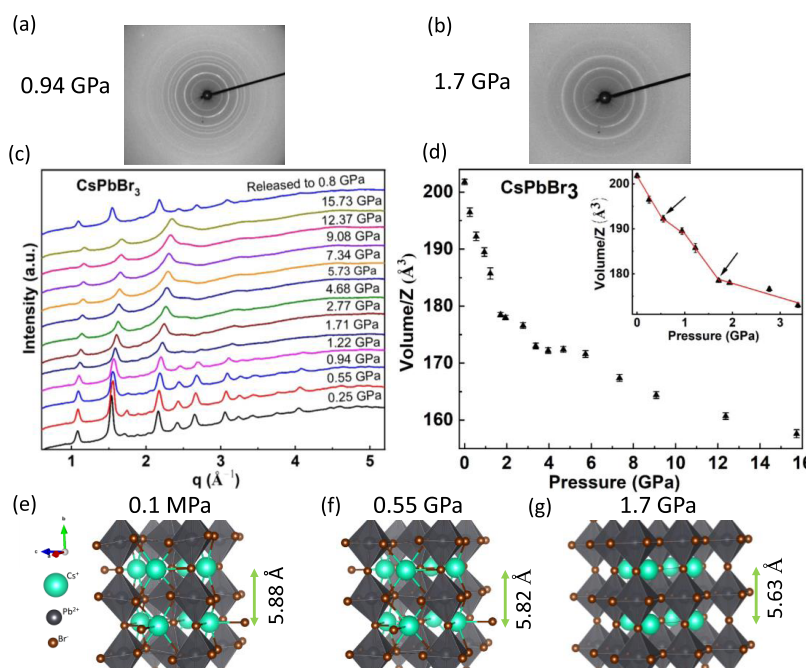


Figure 5. Synchrotron-based XRD from CsPbBr_3 NCs. (a) and (b) 2D XRD images of CsPbBr_3 NCs at 0.94 and 1.7 GPa, respectively. (c) High-pressure synchrotron XRD pattern of CsPbBr_3 NCs. (d) Pressure dependence of volume/Z up to 16 GPa with error bars, where Z, the formula unit, is 4 for the orthorhombic phase and 1 for the cubic phase. The pressure versus volume/Z up to 3.4 GPa is shown as an inset for clarity. The slanted arrows represent the volume anomalies and the red line is a guide to the eye. (e–g) Crystal structure of CsPbBr_3 at 0.1 MPa, 0.55 GPa, and 1.7 GPa, respectively. The Cs^+ , Pb^{2+} , and Br^- ions are represented by green, black, and brown colors, respectively. The distance between adjacent Cs atoms along *b* direction is depicted by double-sided green arrows.

High-Pressure XRD Measurements. To elucidate the pressure-induced changes observed in the PL spectra, high-pressure synchrotron XRD experiments were carried out. The XRD measurements provide insights into structural phase transitions as a result of the tilting and rotation of $\text{Pb}-\text{Br}_6$ octahedra. The XRD measurements from CsPbBr_3 NCs at ambient pressure confirm that the NCs stabilize in orthorhombic structure with *Pnma* symmetry. The lattice parameters extracted from the ambient XRD pattern with Rietveld refinement are: $a = 8.392(11)$ Å, $b = 11.751(18)$ Å, and $c = 8.185(1)$ Å. Rietveld refinements of both laboratory and synchrotron XRD data of CsPbBr_3 NCs at ambient and at 0.25 GPa, respectively, are shown in the Supporting Information (Figure S3). There are differences in lattice parameters reported in the literature.^{18,41} Since the lattice parameters, a and c , are very close to each other, it is not uncommon that there is a significant fluctuation of one of the lattice parameters, when they are refined together. Further, different synthesis schemes and size distribution of NCs may also have an impact.

Figure 5 presents our results from high-pressure XRD studies of CsPbBr_3 NCs. The high-pressure synchrotron XRD pattern at selected pressures is shown in Figure 5c with the highest pressure being ~ 15 GPa. A close observation of the high-pressure XRD pattern reveals that apart from the usual shortening of *d*-spacing, there is a significant decrease in intensity of the main XRD peaks along with the vanishing of low *d*-spacing peaks above 1.2 GPa, which indicates the commencement of a structural phase transition. Finally, a complete rearrangement of intensities and broadening of the XRD peaks at 1.7 GPa confirms that the phase transition is completed. The high-pressure phase seems to be robust up to the maximum pressure of ~ 15 GPa in this study. The

broadening of the XRD peaks of the high-pressure phase suggests a loss in long-range order.

The phase transitions observed in CsPbBr_3 NCs in this work contrast a few investigations. The purification procedure of CsPbBr_3 NCs is as important as the synthesis procedure itself and should not be neglected.⁴² Polar solvents, known to remove stabilizing ligands, were used in the purification of CsPbBr_3 NCs in ref 18, which may result in a high NC agglomeration, and the ambient phase is reported to be a mixture of cubic and orthorhombic phases. Their work shows the formation of 2D nanoplatelets under pressure, which again may be facilitated by sintering in one dimension and the ligands being squeezed out in other dimensions. No polar solvents were introduced in the purification step of CsPbBr_3 NCs in this work, resulting in densely passivated surfaces, which hinder agglomeration processes, and the NCs are in the orthorhombic phase at ambient pressure.

The XRD pattern of the CsPbBr_3 NCs at 1.7 GPa has been carefully analyzed to resolve the high-pressure phase. By inspecting group–subgroup relations of the aristotype $\text{Pm}\bar{3}m$ cubic symmetry to account for probable structures, which is derived by tilting of the $\text{Pb}-\text{Br}_6$ octahedra, 15 such possibilities are found.⁴³ Interestingly, the presence of a fewer number of peaks in the XRD pattern at 1.7 GPa compared to lower pressures suggests that the plausible lattice is cubic with either $\text{Im}\bar{3}$ [Glazer tilt notation: $a^+a^+a^+$] or $\text{Pm}\bar{3}m$ symmetry [Glazer tilt notation: $a^0a^0a^0$]. Furthermore, based on the group–subgroup relationship, we rule out the possibility of a hexagonal $\text{P}6_3/mmc$ symmetry as well, which has been proposed in a recent theoretical prediction.¹⁹ The Le Bail fitting of the lattice parameters generated from the XRD pattern at 1.7 GPa with $\text{Im}\bar{3}$ space group produces additional reflections due to the doubling of the prototype cubic unit cell,

which are not experimentally observed. The Rietveld refinement shows that the $Pm\bar{3}m$ space group matches well with the XRD pattern. This space group may be further inferred from recent high-pressure Raman scattering investigations of $CsPbBr_3$ NCs by Zhang et al., where the Raman mode due to the $Pb-Br_6$ vibration disappears at 1.4 GPa.¹⁷ When $CsPbBr_3$ NCs stabilize in the cubic $Pm\bar{3}m$ symmetry, all of the six bromine atoms are equidistant from the central Pb atom. The vibrational frequency originating from the $Pb-Br_6$ octahedron, thus, becomes Raman inactive as the first-order Raman scattering associated with an inversion symmetry vanishes due to the selection rules. We, therefore, assign the high-pressure phase of $CsPbBr_3$ to the $Pm\bar{3}m$ space group, and the refined lattice parameter derived from the XRD pattern at 1.7 GPa is $5.63(8)$ Å (Figure S4). Even though a similar transition was observed in prior reports, the authors claimed the transition to be isostructural rather than a structural phase transition.^{14,17,18} The high-pressure XRD measurements conducted here were carried out from diamond anvil cells with neon as the pressure-transmitting medium; hence, there should be no influence of the medium on the perovskite sample. Surprisingly, both the high-temperature (at ~ 130 °C) and the high-pressure (at ~ 1.7 GPa) phases in $CsPbBr_3$ NCs are identical; such a phenomenon is rare in crystallography. Similar observations have been noticed in the noncubic phase of Au microcrystallites.⁴⁴

We plot the pressure-dependent volume (volume per formula unit) in Figure 5d. The pressure-dependent cell parameters are provided in the Supporting Information (Figure S5). As expected, there is an overall decrease in the volume with pressure. However, there are four anomalies observed at 0.5, 1.7, 3.5, and 5.7 GPa. The change at 0.5 GPa can be correlated to the subtle band gap energy change observed in the PL spectra, where the pressure coefficient is seen to change in the 0.3–0.5 GPa range (Figure 3c). This change arises due to changes in bond lengths and bond angles of the orthorhombic lattice with pressure-induced octahedral tilt (see the Supporting Information). The slope changes observed at 3.5 and 5.7 GPa may be correlated to isostructural transition as there is no symmetry change seen from high-pressure XRD above 1.7 GPa. It is worth pointing out that high-pressure *in situ* AC impedance spectroscopy measurements from $CsPbBr_3$ single crystals show a mixed ionic-electronic-type conduction under the ambient condition to a purely electronic conduction above 2.3 GPa with a strong photoresponse at 1.4 GPa.⁴⁵ It is conceivable that the enhancement in photoresponse has its origin in the structural phase transition that we observe at 1.7 GPa in $CsPbBr_3$ NCs. The pressure-induced phase transition from the orthorhombic to the cubic phase is reversible with an approximate change in volume by 3.9%. A systematic decrease in the band gap of the high-pressure $Pm\bar{3}m$ phase, as observed from PL and the theory, along with the stability of this phase, as observed from XRD, signals a probable pressure-induced metallization of this high-pressure phase.

The next question we ask is whether the distinct high-pressure PL behavior of RP- $CsPbBr_3$ NCs can be correlated to its structural changes. Additionally, how does the high-pressure structure of RP- $CsPbBr_3$ NCs compare with that of $CsPbBr_3$ NCs? We anticipate that the presence of RP faults not only provides a route toward enhanced emission under pressure (Figure 3d) but also they clarify the nature of pressure-induced phase transitions in lead halide perovskites, which thus far has not been solved. The nature of the RP planar faults in RP-

$CsPbBr_3$ NCs was earlier studied using scanning transmission electron microscopy and DFT calculations.²³ These faults comprise rock-salt stacking of two $CsBr$ layers.

Figure 6 presents XRD studies of RP- $CsPbBr_3$ NCs. The indexing and Bragg reflections of RP- $CsPbBr_3$ are shown in the

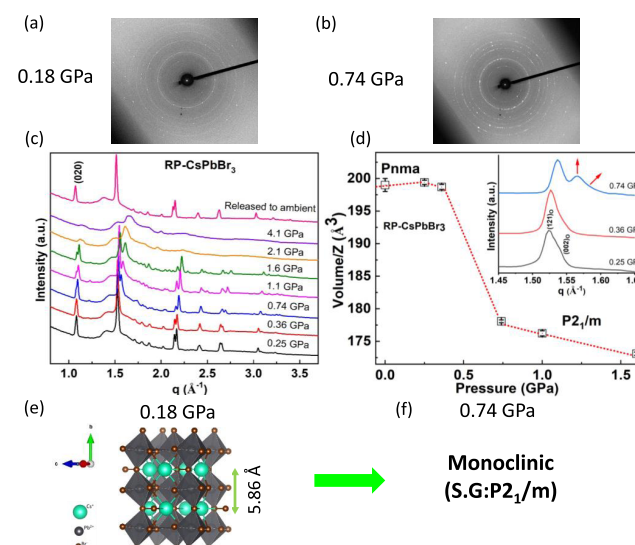


Figure 6. Synchrotron-based XRD from RP- $CsPbBr_3$. (a, b) Two-dimensional XRD images of RP- $CsPbBr_3$ NCs at 0.18 and 0.74 GPa, respectively. (c) High-pressure synchrotron XRD pattern of RP- $CsPbBr_3$ NCs. (d) Pressure dependence of volume/Z with error bars. The dotted red line is guidance to the eye. The (121)_O and (002)_O doublets of RP- $CsPbBr_3$ NCs for selected pressures are shown as an inset. The red arrows at 0.74 GPa indicate the emergence of new peaks or merging of peaks as explained in the text. (e) Crystal structure of RP- $CsPbBr_3$ at 0.18 GPa. The Cs^+ , Pb^{2+} , and Br^- ions are represented by green, black, and brown colors, respectively. (f) The transition from the orthorhombic to the monoclinic ($P2_1/m$) phase at 0.74 GPa is schematically shown by the green arrow.

Supporting Information (Figure S6). Figure 6c shows the XRD pattern of RP- $CsPbBr_3$ for selected pressures. The origin of the broad shoulder below the (121) peak may be attributed to two possibilities. The postsynthesis growth of RP- $CsPbBr_3$ results in a byproduct compound, $C_2H_5-Zn-OOR'$ (where $R' = C_{17}H_{33}$);²² the broad feature could arise from the alkyl chains. Another possibility is due to a sublattice formation by the RP phase as a result of the stacking fault. Such features have been observed in oxide perovskites. A detailed explanation is provided in the Supporting Information.

At ambient pressure, the XRD pattern from RP- $CsPbBr_3$ NCs is highly spotty, which may be ascribed to the single-crystal nature of NCs. It becomes more powder-like after a small compression due to pressure-induced crystallization, which is associated with an increase in the volume of the unit cell till 0.2 GPa (Figure 6d). The calculated lattice parameters of the ambient XRD pattern with orthorhombic $Pnma$ phase using Le Bail fitting are found to be: $a = 8.25(4)$ Å, $b = 11.76(3)$ Å, and $c = 8.21(11)$ Å.

It is evident from the inset of Figure 6d that the shoulder peak (002)_O (where O denotes the orthorhombic phase) around 1.53 \AA^{-1} becomes weak at 0.36 GPa. The emergence of a well-resolved peak at 1.565 \AA^{-1} with a distinct shoulder is observed at 0.74 GPa, as indicated by the red arrows. The shoulder peak becomes prominent at 1.1 GPa. A systematic data processing with careful masking of XRD images confirms

the shoulder at 0.74 GPa to be from the sample. This suggests that the $(002)_0$ peak of the orthorhombic lattice at 0.36 GPa either vanishes or merges with the peak around 1.565 \AA^{-1} at 0.74 GPa. Detailed XRD analysis of RP-CsPbBr₃ is provided in the Supporting Information, which further confirms a symmetry lowering structural transition at 0.74 GPa. The phase transition, thus, observed is associated with defect formation, which is understood by the appearance of multiple spots on the XRD image at 0.74 GPa (Figure 6b).

The high-pressure XRD pattern of RP-CsPbBr₃ NCs is associated with vanishing and broadening of peaks above 1.6 GPa due to a loss of long-range order; the sample thus transforms to an amorphous-like phase, which is in agreement with the changes in PL (Figure 3) where the PL peak disappears above 1.6 GPa. Above 1.1 GPa, the data analysis becomes difficult since a large number of spots appear in the XRD image, which is most likely due to pressure-induced crystallization owing to the formation of additional defects during the structural phase transition. However, the high-pressure phase at 0.74 GPa could be analyzed. The group–subgroup relation of the aristotype $Pm\bar{3}m$ cubic symmetry indicates that $P2_1/m$ is the most probable symmetry for this high-pressure phase [Glazer tilt notation: $a^+b^-c^-$]. The expected lattice parameters and the angle (β) for the $P2_1/m$ symmetry are: $a \simeq \sqrt{2}a_p$, $b \simeq 2a_p$, $c = \sqrt{2}a_p$ and $\beta \neq 90^\circ$, where a_p is the lattice parameter of aristotype $Pm\bar{3}m$ cubic structure.^{8,43} Based on this, we find a suitable lattice for the monoclinic phase with lattice parameters: $a = 8.595(8) \text{ \AA}$, $b = 11.470(6) \text{ \AA}$, $c = 7.265(7)$ and $\beta = 95.95(10)^\circ$ by indexing with the Expo 2014 software.⁴⁶ The Le Bail fitting of the high-pressure monoclinic phase is shown in the Supporting Information (Figure S7), where the changes in the lattice parameters and volume clearly show that the orthorhombic phase is inconsistent with the XRD pattern at 0.74 GPa. The Wyckoff positions of the high-pressure monoclinic phase, however, could not be obtained. Since the volume of the monoclinic phase is very close to that of the orthorhombic phase, we assume the formula unit: $Z = 4$ for the monoclinic phase.

The results obtained from high-pressure XRD of RP-CsPbBr₃ NCs match well with the changes in the PL spectra (Figure 3f). For instance, a dramatic PL intensity drop from the ambient to ~ 0.2 GPa can be correlated to the pressure-induced crystallization changes till 0.2 GPa in XRD. Similarly, the band gap changes at ~ 0.8 GPa in the PL spectra can be interpreted as a consequence of the structural phase transition. Further, the increase in PL intensity at ~ 1 GPa closely follows the pressure-induced monoclinic structural transition. This phase transition is found to be reversible (Figure S9) and accompanied by nearly 10% volume change. The reversibility in the XRD data further suggests that it is unlikely that RP-CsPbBr₃ NCs form nanosheets under pressure. II–VI nanosheet semiconducting NCs, for example, show irreversible phase transformation under pressure.⁴⁷ In contrast to CsPbBr₃ NCs, which undergo a cubic phase transition at high pressure, RP-CsPbBr₃ undergoes a phase transition to the monoclinic phase beyond 0.7 GPa, and by 2 GPa, the long-range order almost disappears.

CONCLUSIONS

In conclusion, pressure-dependent synchrotron XRD investigations from CsPbBr₃ NCs exhibit both isostructural and structural phase transitions. We resolve the structural

transitions under pressure for NCs with and without RP faults. The CsPbBr₃ NCs exhibit isostructural transitions at 0.3 and 0.9 GPa followed by an orthorhombic to cubic $Pm\bar{3}m$ phase transition at 1.7 GPa. The RP-CsPbBr₃ NCs (with the presence of RP faults) exhibit an orthorhombic to monoclinic $P2_1/m$ phase transition at 0.74 GPa, concomitant with a dramatic increase in the PL intensity compared to ambient pressure. The narrowing of the band gap with pressure observed in the theoretical calculations is consistent with the experimental pressure-dependent PL energies. The RP-CsPbBr₃ sample shows nuances of a blue shift of the PL energy beyond 1 GPa. This study suggests that high pressure could serve as a tuning parameter for directing the synthesis of lead halide perovskite NCs and for engineering RP faults to improve the overall optical properties for optoelectronic applications.

ASSOCIATED CONTENT

SI Supporting Information

The Supporting Information is available free of charge at <https://pubs.acs.org/doi/10.1021/acs.chemmater.9b04157>.

Low-magnification high-angle annular dark-field images of RP planar defects in RP-CsPbBr₃ NCs; PL spectra during pressure increasing and decreasing cycles; Le Bail fitting and Rietveld refinement of CsPbBr₃ NCs (with and without RP); pressure-dependent lattice parameters; analysis of orthorhombic to monoclinic phase transition in RP-CsPbBr₃ NCs; bond lengths and bond angles of PbBr₆ octahedra; low-temperature laboratory-based XRD from CsPbBr₃ NCs ([PDF](#))

AUTHOR INFORMATION

Corresponding Author

Suchismita Guha — University of Missouri, Columbia, Missouri; orcid.org/0000-0002-6269-2298; Email: guhas@missouri.edu

Other Authors

Sorb Yesudhas — University of Missouri, Columbia, Missouri

Maria V. Morrell — University of Missouri, Columbia, Missouri

Matthew J. Anderson — University of Missouri, Columbia, Missouri

Carsten A. Ullrich — University of Missouri, Columbia, Missouri

Curtis Kenney-Benson — Argonne National Laboratory, Lemont, Illinois

Yangchuan Xing — University of Missouri, Columbia, Missouri; orcid.org/0000-0002-5985-3222

Complete contact information is available at: <https://pubs.acs.org/10.1021/acs.chemmater.9b04157>

Author Contributions

The manuscript was written through contributions of all authors. All authors have given approval to the final version of the manuscript.

Notes

The authors declare no competing financial interest.

■ ACKNOWLEDGMENTS

We acknowledge the support of this work through the National Science Foundation (NSF) under Grant no. DMR-1807263. C.A.U. and M.J.A. were supported by Department of Energy Grant no. DE-SC0019109 and NSF Grant no. DMR-1810922. Portions of this work were performed at HPCAT (Sector 16), Advanced Photon Source (APS), Argonne National Laboratory. HPCAT operations are supported by DOE-NNSA's Office of Experimental Sciences. The APS is a US Department of Energy (DOE) Office of Science User Facility operated for the DOE Office of Science by Argonne National Laboratory under Contract No. DE-AC02-06CH11357. We thank Ridwan Sakidja for useful discussions, Sergey Tkachev, GSECARS, APS for Ne gas loading in the DAC, Changyong Park for ambient pressure XRD measurements, and Steven Kelley for low T laboratory-based XRD measurements.

■ REFERENCES

- (1) Stoumpos, C. C.; Kanatzidis, M. G. The Renaissance of Halide Perovskites and Their Evolution as Emerging Semiconductors. *Acc. Chem. Res.* **2015**, *48*, 2791–2802.
- (2) Protesescu, L.; Yakunin, S.; Bodnarchuk, M. I.; Krieg, F.; Caputo, R.; Hendon, C. H.; Yang, R. X.; Walsh, A.; Kovalenko, M. V. Nanocrystals of Cesium Lead Halide Perovskites (CsPbX_3 , X = Cl, Br, and I): Novel Optoelectronic Materials Showing Bright Emission with Wide Color Gamut. *Nano Lett.* **2015**, *15*, 3692–3696.
- (3) Yakunin, S.; Protesescu, L.; Krieg, F.; Bodnarchuk, M. I.; Nedelcu, G.; Humer, M.; De Luca, G.; Fiebig, M.; Heiss, W.; Kovalenko, M. V. Low-threshold amplified spontaneous emission and lasing from colloidal nanocrystals of caesium lead halide perovskites. *Nat. Commun.* **2015**, *6*, No. 8056.
- (4) Liu, F.; Zhang, Y.; Ding, C.; Kobayashi, S.; Izuishi, T.; Nakazawa, N.; Toyoda, T.; Ohta, T.; Hayase, S.; Minemoto, T.; Yoshino, K.; Dai, S.; Shen, Q. Highly Luminescent Phase-Stable CsPbI_3 Perovskite Quantum Dots Achieving Near 100% Absolute Photoluminescence Quantum Yield. *ACS Nano* **2017**, *11*, 10373–10383.
- (5) Akkerman, Q. A.; Rainò, G.; Kovalenko, M. V.; Manna, L. Genesis, challenges and opportunities for colloidal lead halide perovskite nanocrystals. *Nat. Mater.* **2018**, *17*, 394–405.
- (6) Gong, M.; Sakidja, R.; Goul, R.; Ewing, D.; Casper, M.; Stramal, A.; Elliot, A.; Wu, J. Z. High-Performance All-Inorganic CsPbCl_3 Perovskite Nanocrystal Photodetectors with Superior Stability. *ACS Nano* **2019**, *13*, 1772–1783.
- (7) Young, J.; Rondinelli, J. M. Octahedral Rotation Preferences in Perovskite Iodides and Bromides. *J. Phys. Chem. Lett.* **2016**, *7*, 918–922.
- (8) Woodward, P. Octahedral Tilting in Perovskites. I. Geometrical Considerations. *Acta Crystallogr., Sect. B: Struct. Sci.* **1997**, *53*, 32–43.
- (9) Cottingham, P.; Brutchev, R. L. Depressed Phase Transitions and Thermally Persistent Local Distortions in CsPbBr_3 Quantum Dots. *Chem. Mater.* **2018**, *30*, 6711–6716.
- (10) Stoumpos, C. C.; Malliakas, C. D.; Peters, J. A.; Liu, Z.; Sebastian, M.; Im, J.; Chasapis, T. C.; Wibowo, A. C.; Chung, D. Y.; Freeman, A. J.; Wessels, B. W.; Kanatzidis, M. G. Crystal Growth of the Perovskite Semiconductor CsPbBr_3 : A New Material for High-Energy Radiation Detection. *Cryst. Growth Des.* **2013**, *13*, 2722–2727.
- (11) Hirotsu, S.; Harada, J.; Iizumi, M.; Gesi, K. Structural Phase Transitions in CsPbBr_3 . *J. Phys. Soc. Jpn.* **1974**, *37*, 1393–1398.
- (12) Mujica, A.; Rubio, A.; Muñoz, A.; Needs, R. J. High-pressure phases of group-IV, III–V, and II–VI compounds. *Rev. Mod. Phys.* **2003**, *75*, 863–912.
- (13) Knaapila, M.; Guha, S. Blue emitting organic semiconductors under high pressure: status and outlook. *Rep. Prog. Phys.* **2016**, *79*, No. 066601.
- (14) Xiao, G.; Cao, Y.; Qi, G.; Wang, L.; Liu, C.; Ma, Z.; Yang, X.; Sui, Y.; Zheng, W.; Zou, B. Pressure Effects on Structure and Optical Properties in Cesium Lead Bromide Perovskite Nanocrystals. *J. Am. Chem. Soc.* **2017**, *139*, 10087–10094.
- (15) Beimborn, J. C.; Hall, L. M. G.; Tongying, P.; Dukovic, G.; Weber, J. M. Pressure Response of Photoluminescence in Cesium Lead Iodide Perovskite Nanocrystals. *J. Phys. Chem. C* **2018**, *122*, 11024–11030.
- (16) Zhang, L.; Wang, L.; Wang, K.; Zou, B. Pressure-Induced Structural Evolution and Optical Properties of Metal-Halide Perovskite CsPbCl_3 . *J. Phys. Chem. C* **2018**, *122*, 15220–15225.
- (17) Zhang, L.; Zeng, Q.; Wang, K. Pressure-Induced Structural and Optical Properties of Inorganic Halide Perovskite CsPbBr_3 . *J. Phys. Chem. Lett.* **2017**, *8*, 3752–3758.
- (18) Nagaoka, Y.; Hills-Kimball, K.; Tan, R.; Li, R.; Wang, Z.; Chen, O. Nanocube Superlattices of Cesium Lead Bromide Perovskites and Pressure-Induced Phase Transformations at Atomic and Mesoscale Levels. *Adv. Mater.* **2017**, *29*, No. 1606666.
- (19) Huang, Y.; Wang, L.; Ma, Z.; Wang, F. Pressure-Induced Band Structure Evolution of Halide Perovskites: A First-Principles Atomic and Electronic Structure Study. *J. Phys. Chem. C* **2019**, *123*, 739–745.
- (20) Zhao, Y.-Q.; Ma, Q.-R.; Liu, B.; Yu, Z.-L.; Cai, M.-Q. Pressure-induced strong ferroelectric polarization in tetra-phase perovskite CsPbBr_3 . *Phys. Chem. Chem. Phys.* **2018**, *20*, 14718–14724.
- (21) Yu, Y.; Zhang, D.; Yang, P. Ruddlesden–Popper Phase in Two-Dimensional Inorganic Halide Perovskites: A Plausible Model and the Supporting Observations. *Nano Lett.* **2017**, *17*, 5489–5494.
- (22) Morrell, M. V.; He, X.; Luo, G.; Thind, A. S.; White, T. A.; Hachtel, J. A.; Borisevich, A. Y.; Idrobo, J.-C.; Mishra, R.; Xing, Y. Significantly Enhanced Emission Stability of CsPbBr_3 Nanocrystals via Chemically Induced Fusion Growth for Optoelectronic Devices. *ACS Appl. Nano Mater* **2018**, *1*, 6091–6098.
- (23) Thind, A. S.; Luo, G.; Hachtel, J. A.; Morrell, M. V.; Cho, S. B.; Borisevich, A. Y.; Idrobo, J.-C.; Xing, Y.; Mishra, R. Atomic Structure and Electrical Activity of Grain Boundaries and Ruddlesden–Popper Faults in Cesium Lead Bromide Perovskite. *Adv. Mater.* **2019**, *31*, No. 1805047.
- (24) Ruddlesden, S. N.; Popper, P. New compounds of the K_2NIF_4 type. *Acta Crystallogr.* **1957**, *10*, 538–539.
- (25) Birol, T.; Benedek, N. A.; Fennie, C. J. Interface Control of Emergent Ferroic Order in Ruddlesden–Popper $\text{Sr}_{n+1}\text{Ti}_n\text{O}_{3n+1}$. *Phys. Rev. Lett.* **2011**, *107*, No. 257602.
- (26) Tsai, H.; Nie, W.; Blancon, J.-C.; Stoumpos, C. C.; Asadpour, R.; Harutyunyan, B.; Neukirch, A. J.; Verduzco, R.; Crochet, J. J.; Tretiak, S.; Pedesseau, L.; Even, J.; Alam, M. A.; Gupta, G.; Lou, J.; Ajayan, P. M.; Bedzyk, M. J.; Kanatzidis, M. G.; Mohite, A. D. High-efficiency two-dimensional Ruddlesden–Popper perovskite solar cells. *Nature* **2016**, *536*, 312.
- (27) Tsai, H.; Nie, W.; Blancon, J.-C.; Stoumpos, C. C.; Soe, C. M. M.; Yoo, J.; Crochet, J.; Tretiak, S.; Even, J.; Sadhanala, A.; Azzellino, G.; Brenes, R.; Ajayan, P. M.; Bulović, V.; Stranks, S. D.; Friend, R. H.; Kanatzidis, M. G.; Mohite, A. D. Stable Light-Emitting Diodes Using Phase-Pure Ruddlesden–Popper Layered Perovskites. *Adv. Mater.* **2018**, *30*, No. 1704217.
- (28) Hammersley, A. P.; Svensson, S. O.; Hanfland, M.; Fitch, A. N.; Hausermann, D. Two-dimensional detector software: From real detector to idealised image or two-theta scan. *High Pressure Res.* **1996**, *14*, 235–248.
- (29) Rodríguez-Carvajal, J. Recent advances in magnetic structure determination by neutron powder diffraction. *Phys. B* **1993**, *192*, 55–69.
- (30) Gonze, X.; Amadon, B.; Anglade, P. M.; Beuken, J. M.; Bottin, F.; Boulanger, P.; Bruneval, F.; Caliste, D.; Caracas, R.; Côté, M.; Deutsch, T.; Genovese, L.; Ghosez, P.; Giantomassi, M.; Goedecker, S.; Hamann, D. R.; Hermet, P.; Jollet, F.; Jomard, G.; Leroux, S.; Mancini, M.; Mazevert, S.; Oliveira, M. J. T.; Onida, G.; Pouillon, Y.; Rangel, T.; Rignanese, G. M.; Sangalli, D.; Shaltaf, R.; Torrent, M.; Verstraete, M. J.; Zerah, G.; Zwanziger, J. W. ABINIT: First-principles approach to material and nanosystem properties. *Comput. Phys. Commun.* **2009**, *180*, 2582–2615.

(31) Gonze, X.; Jollet, F.; Abreu Araujo, F.; Adams, D.; Amadon, B.; Appelcourt, T.; Audouze, C.; Beuken, J. M.; Bieder, J.; Bokhanchuk, A.; Bousquet, E.; Bruneval, F.; Caliste, D.; Côté, M.; Dahm, F.; Da Pieve, F.; Delaveau, M.; Di Gennaro, M.; Dorado, B.; Espejo, C.; Geneste, G.; Genovese, L.; Gerossier, A.; Giantomassi, M.; Gillet, Y.; Hamann, D. R.; He, L.; Jomard, G.; Laflamme Janssen, J.; Le Roux, S.; Levitt, A.; Lherbier, A.; Liu, F.; Lukačević, I.; Martin, A.; Martins, C.; Oliveira, M. J. T.; Poncé, S.; Pouillon, Y.; Rangel, T.; Rignanese, G. M.; Romero, A. H.; Rousseau, B.; Rubel, O.; Shukri, A. A.; Stankovski, M.; Torrent, M.; Van Setten, M. J.; Van Troeye, B.; Verstraete, M. J.; Waroquiers, D.; Wiktor, J.; Xu, B.; Zhou, A.; Zwanziger, J. W. Recent developments in the ABINIT software package. *Comput. Phys. Commun.* **2016**, *205*, 106–131.

(32) Hamann, D. R. Optimized norm-conserving Vanderbilt pseudopotentials. *Phys. Rev. B* **2013**, *88*, No. 085117.

(33) Perdew, J. P.; Burke, K.; Ernzerhof, M. Generalized Gradient Approximation Made Simple. *Phys. Rev. Lett.* **1996**, *77*, 3865–3868.

(34) Monkhorst, H. J.; Pack, J. D. Special points for Brillouin-zone integrations. *Phys. Rev. B* **1976**, *13*, 5188–5192.

(35) Diroll, B. T.; Zhou, H.; Schaller, R. D. Low-Temperature Absorption, Photoluminescence, and Lifetime of CsPbX₃ (X = Cl, Br, I) Nanocrystals. *Adv. Funct. Mater.* **2018**, *28*, No. 1800945.

(36) Lan, S.; Li, W.; Wang, S.; Li, J.; Wang, J.; Wang, H.; Luo, H.; Li, D. Vapor-Phase Growth of CsPbBr₃ Microstructures for Highly Efficient Pure Green Light Emission. *Adv. Opt. Mater.* **2019**, *7*, No. 1801336.

(37) Guha, S.; Cai, Q.; Chandrasekhar, M.; Chandrasekhar, H. R.; Kim, H.; Alvarenga, A. D.; Vogelgesang, R.; Ramdas, A. K.; Melloch, M. R. Photoluminescence of short-period GaAs/AlAs superlattices: A hydrostatic pressure and temperature study. *Phys. Rev. B* **1998**, *58*, 7222–7229.

(38) Brown, J.; Elsass, C.; Poblenz, C.; Petroff, P. M.; Speck, I. S. Temperature Dependent Photoluminescence of MBE Grown Gallium Nitride Quantum Dots. *Phys. Status Solidi B* **2001**, *228*, 199–202.

(39) Liao, M.; Shan, B.; Li, M. In Situ Raman Spectroscopic Studies of Thermal Stability of All-Inorganic Cesium Lead Halide (CsPbX₃, X = Cl, Br, I) Perovskite Nanocrystals. *J. Phys. Chem. Lett.* **2019**, *10*, 1217–1225.

(40) Bertolotti, F.; Protesescu, L.; Kovalenko, M. V.; Yakunin, S.; Cervellino, A.; Billinge, S. J. L.; Terban, M. W.; Pedersen, J. S.; Masciocchi, N.; Guagliardi, A. Coherent Nanotwins and Dynamic Disorder in Cesium Lead Halide Perovskite Nanocrystals. *ACS Nano* **2017**, *11*, 3819–3831.

(41) Cottingham, P.; Brutchey, R. L. On the crystal structure of colloidally prepared CsPbBr₃ quantum dots. *Chem. Commun.* **2016**, *S2*, S246–S249.

(42) Li, J.; Xu, L.; Wang, T.; Song, J.; Chen, J.; Xue, J.; Dong, Y.; Cai, B.; Shan, Q.; Han, B.; Zeng, H. 50-Fold EQE Improvement up to 6.27% of Solution-Processed All-Inorganic Perovskite CsPbBr₃ QLEDs via Surface Ligand Density Control. *Adv. Mater.* **2017**, *29*, No. 1603885.

(43) Howard, C. J.; Stokes, H. T. Group-Theoretical Analysis of Octahedral Tilting in Perovskites. *Acta Crystallogr., Sect. B: Struct. Sci.* **1998**, *54*, 782–789.

(44) Mettela, G.; Sorb, Y. A.; Shukla, A.; Bellin, C.; Svitlyk, V.; Mezouar, M.; Narayana, C.; Kulkarni, G. U. Extraordinarily Stable Noncubic Structures of Au: A High-Pressure and -Temperature Study. *Chem. Mater.* **2017**, *29*, 1485–1489.

(45) Ou, T.; Liu, C.; Yan, H.; Han, Y.; Wang, Q.; Liu, X.; Ma, Y.; Gao, C. Effects of pressure on the ionic transport and photoelectrical properties of CsPbBr₃. *Appl. Phys. Lett.* **2019**, *114*, No. 062105.

(46) Altomare, A.; Cuocci, C.; Giacovazzo, C.; Moliterni, A.; Rizzi, R.; Corriero, N.; Falcicchio, A. EXPO2013: a kit of tools for phasing crystal structures from powder data. *J. Appl. Crystallogr.* **2013**, *46*, 1231–1235.

(47) Wang, Z.; Wen, X.-D.; Hoffmann, R.; Son, J. S.; Li, R.; Fang, C.-C.; Smilgies, D.-M.; Hyeon, T. Reconstructing a solid-solid phase transformation pathway in CdSe nanosheets with associated soft ligands. *Proc. Natl. Acad. Sci. USA* **2010**, *107*, 17119–17124.